Review of Scientific Instruments ARTICLE pubs.aip.org/aip/rsi

Refurbishment and commissioning of a dual-band 23/31 GHz tipping radiometer at potential radio astronomical sites

Cite as: Rev. Sci. Instrum. 96, 044503 (2025); doi: 10.1063/5.0239476
Submitted: 19 September 2024 • Accepted: 29 March 2025 •
Published Online: 22 April 2025

J. Cuazoson,[1,a] D. Hiriart,[2] T. Stander,[3] R. Botha,[4] J. Contreras,[5] D. Ferrusca,[5] E. Ibarra-Medel,[5] S. Kurtz,[1] R. Neate,[3] D. Rojas,[2] and M. Velázquez[5]

AFFILIATIONS

[1] Instituto de Radioastronomía y Astrofísica, Universidad Nacional Autónoma de Mexico, Morelia, Mexico
[2] Instituto de Astronomía, Universidad Nacional Autónoma de Mexico, Ensenada, Mexico
[3] Department EEC Engineering, University of Pretoria, Pretoria, South Africa
[4] South African Radio Astronomy Observatory, River Park Liesbeek Parkway, Settlers Way, Cape Town 7705, South Africa
[5] Instituto Nacional de Astrofísica Óptica y Electrónica, Tonantzintla, Mexico

[a] **Author to whom correspondence should be addressed:** j.cuazoson@irya.unam.mx

ABSTRACT

This paper reports on the refurbishment of a dual-band 23/31 GHz tipping radiometer previously used to measure atmospheric water vapor content at the Hartebeesthoek Radio Astronomy Observatory. We describe the motivation for the refurbishment, provide technical details of the modifications made to the instrument, and present preliminary test results of field measurements at the site of the High Energy Stereoscopic System Observatory in Namibia. Together with other radiometric measurements, this instrument will contribute to the site characterization of potential radio astronomical observatories in southern Africa.

I. BACKGROUND

Radio astronomy observations, especially in microwaves, are heavily affected by tropospheric water vapor,[1] limiting both source brightness measurements and phase coherence in radio interferometry observations. To address these issues, water vapor radiometers (WVRs)[2–4] are frequently deployed at radio astronomy observatories to measure precipitable water vapor (PWV) as an aid for data calibration and telescope management. WVRs are also often deployed to characterize the long-term atmospheric opacity at candidate telescope sites prior to the construction of new radio astronomy facilities, such as the proposed African Millimeter Telescope (AMT)[5] or the Next-Generation Very Large Array (ngVLA).[6]

The main atmospheric water vapor emission lines in the microwave range occur at 22.235 and 183.31 GHz.[7] Both lines can be used to trace the atmospheric water vapor content, but generally, the observation band and the geographical location of the observatory determine the use of a cm-wave or a mm-wave WVR.[8] Several WVR architectures can be found in the literature, e.g., single-band,[9,10] multiple-band,[11,12] system-on-chip-based,[13–15] and spectrometer-based,[16,17] whose designs depend not only on the scientific applications of the instrument but also on the water vapor emission line to be characterized.

The Hartebeesthoek Radio Astronomy Observatory (HartRAO) of the South African Radio Astronomy Observatory acquired the Generation III tipping radiometer WVR-III[18] in the early 2000s to measure the atmospheric water vapor. This device was developed by the Federal Institute of Technology (ETH Zurich) of Switzerland in cooperation with CAPTEC GmbH: the former was in charge of mechanism control, communication interfaces, data acquisition, and instrument calibration, and the latter was in charge of mechanical design, construction, and documentation. The HartRAO application of the WVR-III was for path delay correction in satellite geodesy: because atmospheric path delay is related to the water vapor

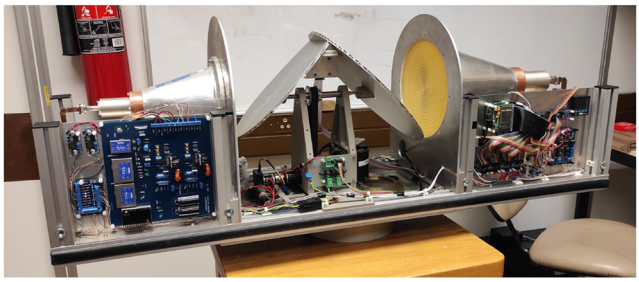

FIG. 1. Testing the WVR-III+ at the Carl Emily Fuchs Institute for Microelectronics (University of Pretoria) in November 2021.

content, the measurements of PWV may be used to effect a delay correction.

The WVR-III aided several observational campaigns from 2000 to 2007 at HartRAO prior to suffering numerous failures in power supplies, control systems, data acquisition electronics, and various other circuits. Under the joint South Africa–Mexico Bilateral Programme on Water Vapor Radiometry[19] (SA-MX), this instrument was refurbished over the course of 2019–2021 and renamed as WVR-III+, with preliminary efforts in this regard previously reported in 2020.[20] The WVR-III+ was returned to the University of Pretoria in mid-2021 (see Fig. 1) and recommissioned at HartRAO in early 2022. After several months, the radiometer was moved to the High Energy Spectroscopic System (H.E.S.S.) in Namibia as part of the site characterization tasks for the AMT project. We report here on the detailed refurbishment of this instrument, including requalification data taken at the H.E.S.S. site[21] in the second half of 2022.

II. PRINCIPLE OF OPERATION

In the following, we describe the basis of atmospheric measurements using a ground-based microwave radiometer. We rely on the techniques described here and implement them on the refurbished WVR-III+.

A. Measuring the atmospheric brightness temperature

The objective of a radiometer is to measure the intensity of incident microwave radiation, which is then expressed as a brightness temperature. This is accomplished by measuring the atmospheric scene intensity and then retrieving the brightness temperature by performing a Y-factor measurement with two targets at known (hot and cold) temperatures. Figure 2 presents a simplified radiometer block diagram in which the microwave radiation coming from the atmosphere is received by the feed horn and preamplified and then down-converted in frequency for acquisition. The signal is amplified again and passed to a bandpass filter to limit the frequency response. Then, a square-law detector provides a DC signal proportional to the noise power of the incoming signal, which in turn is proportional to the atmospheric brightness temperature. Finally, a computer acquires the radiometer output for signal processing and data retrieval.

The system corrects errors caused by gain drifts by comparing the incident radiation power with that of a cold and hot calibration load. A noise source is used as a hot (*on*) and cold (*off*) load, equivalent to a temperature of several thousand kelvin in the *on* state. The hot load power T_H is lowered by an attenuator to have a value approximately equal to the antenna (*sky*) noise power, improving the linear response of the detector. When the noise source is *off*, the cold noise temperature T_C corresponds to its physical temperature (~300 K). Assuming a linear response, this results in a relationship between the measured output voltages and the antenna temperature (T_A) as

$$T_A = \frac{V_A - V_C}{V_H - V_C}(T_H - T_C) + T_C, \tag{1}$$

where V_A, V_H, and V_C are the measured output voltages of the antenna, hot load, and cold load, respectively. The observing cycle is performed on a relatively short time scale and alternates between measuring the power level of the cold load, the hot load, and the sky. The variation caused by the gain drifts, which have a time constant much longer than the measurement cycle, is effectively removed by using this method.

B. Measuring atmospheric path delay and PWV

Due to the phenomenon of refraction, electromagnetic signals traversing the Earth's atmosphere experience a modification in their path length, commonly referred to as *path delay*. This refraction is caused by several physical mechanisms, but the interaction with atmospheric water vapor is responsible for a considerable part of the change in the path length.[22] Measurements in radio interferometry and satellite geodesy are disturbed by this increase in path length, and hence, a means for measuring and correcting for the path delay is needed.

The wet path delay (WPD) of an electromagnetic wave is influenced by the amount of water vapor in the atmosphere as

$$WPD = k \int_0^\infty \frac{\rho}{T}\, ds, \tag{2}$$

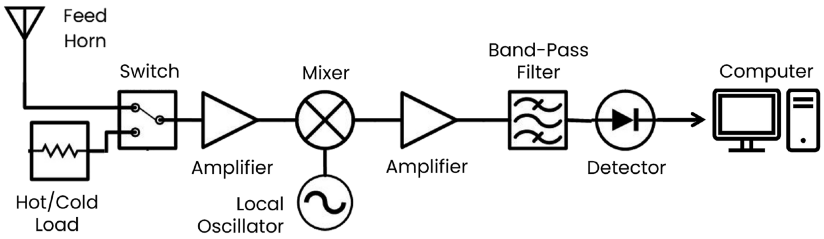

FIG. 2. Generic total power radiometer block diagram.

where ρ and T are the water vapor density and temperature along the path, respectively, and $k = 1.723 \times 10^{-3}$ K/(g/m^3).[23] The path delay can be calculated according to Eq. (2) if the water vapor and temperature profiles along the path s are known. Such profiles can be obtained via balloon radiosondes. Although this technique is straightforward, in practice, it is rarely feasible because atmospheric conditions can change on fairly short timescales, and repeated balloon launches are too slow and expensive to track these changes. An alternative approach to determining the WPD is the use of microwave radiometry.

The relationship between the path delay and the microwave emission of water is a linear function of the brightness temperatures at two different frequencies, $T_B(\nu_1)$ and $T_B(\nu_2)$, such that[24]

$$WPD = a_0 + a_1\ T_B(\nu_1) + a_2\ T_B(\nu_2), \tag{3}$$

in which $\nu_1 < \nu_2$, and the coefficients a_i $(i = 0, 1, 2)$ must be determined for each location by fitting data from radiosondes to the linearized brightness temperatures at a specific pair of frequencies. The lower frequency is intended to probe the water vapor contribution while the higher frequency traces the liquid water component. The former version of the radiometer, WVR-III, used the coefficients provided by ETH Zurich/CAPTEC. In this sense, various combinations of frequency pairs ν_1 and ν_2 have been suggested in the literature,[24] such as 20.3/31.4, 20.0/26.5, or 24.5/31.4 GHz, offering an accuracy of <2 cm in the estimation of the WPD for elevation angles > 15°. During the construction and design by ETH Zurich/CAPTEC, the selected frequency pair was 23.8/31.65 GHz for the WVR-III, giving the atmospheric brightness temperature at each of these frequencies.

Using a model for the microwave atmospheric brightness temperature as a function of PWV and measuring T_B at a frequency close to the water vapor line at 22.235 GHz provides, as a first approximation, the amount of atmospheric water vapor through a linear relation,[25]

$$T_B(\nu) = \alpha_\nu + \beta_\nu PWV, \tag{4}$$

where α_ν is the brightness temperature contribution due to oxygen and β_ν is the conversion factor from PWV to brightness temperature, given in K/mm.

The simultaneous measurements of the atmospheric emission at the two frequencies of the WVR-III+ may also be used as a check of the accuracy of the model used for the atmospheric emission by noting if the results from the two frequencies are consistent with the derived PWV value. Measurement of the sky brightness temperature over a range of elevation angles provides a means to calculate the zenith opacity of the atmosphere,[26] which is a fundamental parameter for the characterization of astronomical sites.

C. Instrumental calibration via tip curve analysis

The conversion from the measured atmospheric emission by the WVR-III+ to linearized brightness temperatures is calculated following the literature.[23] Here, we summarize the salient points.

For a linear detector, two reference points are sufficient to define a linear temperature scale such as kelvins. In the case of a radiometer, time and temperature-dependent drifts of front-end gain and reference loads, system voltages, or a myriad of other parameters result in a continually changing instrumental response. To effect a real-time calibration of the radiometer, perhaps the most commonly used approach is tipping scans.[27] In this procedure, multiple measurements are made over a range of elevation angles, and a subsequent linear fit to these values is used to determine the calibration factors to be applied to the data. In the case of WVR-III+, which has fixed feed horns for both frequencies, a pair of tipping mirrors rotates synchronously to provide for observations at various elevation angles.

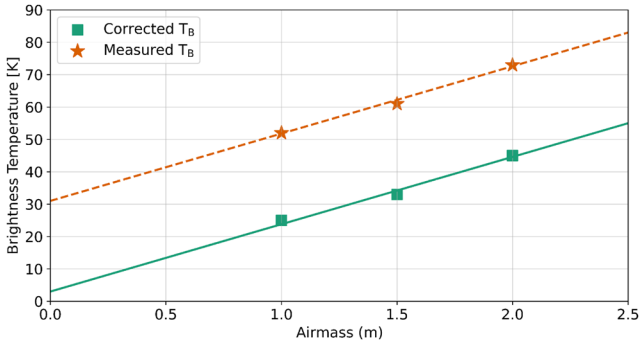

FIG. 3. Tipping curve of the sky brightness temperature (T_B) as a function of air mass (m) without the hot load correction (*orange dashed line*) and with the hot load correction (*turquoise solid line*), required to give the desired zero air mass intercept of T_B = 2.7 K.

In particular, although the hot calibration load has a constant noise temperature, its precise value is not accurately known. Thus, the hot load temperature has to be calibrated using an independent method. A well-known means for performing this calibration is to use the isotropic nature of the cosmic microwave background radiation (CMB), which has a brightness temperature of 2.7 K. In particular, T_B measurements at all elevation angles will have the same contribution from the CMB, therefore, providing an independent means of calibrating the temperature scale.[23]

The radiometer tipping curves are calculated using the assumption that the measured brightness temperature can be represented as a linear function of the air mass m. Initially, a linear fit can be calculated and then extrapolated to $m = 0$. This fit will register a $T_B > 2.7$ K for $m = 0$, and the data points are initially shifted downward by the offset from $T_B(m = 0) = 2.7$ K. This correction factor is referred to as the "hot load correction," ΔT_H, and is added to the hot load temperature. The linear regression of the brightness temperature is then calculated iteratively with new hot load corrections until the y-intercept reaches $T_B(m = 0) = 2.7$ K. The determination of the hot load correction is achieved by measuring three distinct elevations for each tipping curve. Figure 3 shows the tipping curve as an example of a full-sky tip observation. The dashed line in this figure corresponds to the initial linear function that best fits the observations, in a weighted least-squares sense. The solid line is the result after several hot load corrections have been applied.

Direct calibration by means of physical blackbody targets at known temperatures is a viable alternative for the radiometer calibration. Compared to direct physical calibration, the tip curve procedure that we adopt offers the primary advantage that it avoids the complications of including mechanical means for inserting

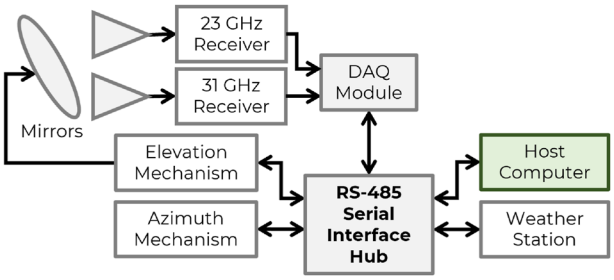

FIG. 4. Original WVR-III architecture.

TABLE I. Technical specifications of the WVR-III+ receivers.[a]

Feature	Receiver 1	Receiver 2	Units
Center frequency	23.8	31.65	GHz
Local oscillator	23.69	31.54	GHz
Intermediate frequency (IF)	110	110	MHz
Bandwidth	200	200	MHz
Noise temperature (DSB)	700	900	K
Half-power beam width (HPBW)[b]	4.3	5.1	°

[a]Provided by ETH Zurich/CAPTEC.
[b]Gaussian beam profile.

blackbody absorbers in the signal path and of maintaining these absorbers at carefully controlled temperatures, both of which would add significant complexity to the instrument.

III. INSTRUMENT DESCRIPTION AND INITIAL CONDITION

The original architecture of the WVR-III was based on a decentralized embedded system, as shown in Fig. 4. An external host computer controls and communicates with all the subsystems of the radiometer via an RS-485 Serial Interface Hub. The signal acquisition of the front-ends and the switching control were done by a microcontroller-based data acquisition module (DAQ), whereas the tipping (allowing elevation and azimuth rotation) was done by two independent complex programmable logic devices (CPLDs). The host computer was provided with a LabVIEW-based graphical interface, which allowed the acquisition and processing of the radiometric data, retrieval of PWV, atmospheric opacity, phase delay, recording of weather variables, and general instrument management. This architecture performed automated tip scans[26] for real-time determination of precipitable water vapor and path delay retrieval using the supplied software. In addition, the graphical interface provided flexible scan scheduling and convenient data accessibility.

The original radio frequency (RF) electronics of the WVR-III are shown in Fig. 5. The receivers are centered at 23.8 and 31.65 GHz, respectively, and are based on a load-switching architecture, similar to the one discussed in Sec. II A. They each consist of a single front-end amplification and downconversion stage, but the 23.8 GHz receiver has a Gunn oscillator tuned at 23.69 GHz, whereas the 31.65 GHz receiver's is tuned at 31.54 GHz. The RF amplification and downconversion in each band is carried out by a low-noise block converter (LNB in Fig. 5) provided by Spacek Labs, model P23-5 for the 23 GHz band and model P31-5 for the 31 GHz band, each featuring ~25 dB downconversion gain and a noise figure of 3.5 dB. The detection blocks (DC Amp in Fig. 5) consist of tunnel diode-based square-law detectors in a series with OP07 operational amplifiers. Switches A (MRI-SPSTK in receiver 1, MRI-SPSTR in receiver 2) and B (QuinStar QSD K-band in receiver 1 and QuinStar QSD Ka-band in receiver 2) were controlled by the DAQ module, which was also responsible for acquiring and transmitting the signals from the receivers to the host computer via the RS-485 interface.

The main technical details of the receivers are listed in Table I. As can be seen, the output noise power is integrated over a 200 MHz bandwidth in each channel. The WVR-III observation sequence followed the scheme discussed in Sec. II A and is now implemented in WVR-III+, as described in Sec. IV B 2.

The WVR-III was sent to Mexico and arrived in early 2019, where the Mexican team started the refurbishment. At that point, several technical tests were done to evaluate the physical status of the radiometer. As a result, we decided to replace many of the radiometer components, primarily due to the lack of technical details of the hardware and the absence of the software source code. The exceptions were the receivers, optics, and associated mechanical controllers, which were fully functional, but some of their components also lacked part or serial numbers, making it difficult for us to directly ascertain the features mentioned in the user manual provided by HartRAO. After testing the front-ends, measurements were obtained within the range specified by the manufacturers. We take this fact as a decisive point to not modify this analog front-end from the original design. In contrast, most of the control electronics were either non-functional or outdated and were completely replaced. In this regard, we proposed a new architecture based on a single-board computer (SBC), which allows a single processing unit to execute all the radiometer tasks that

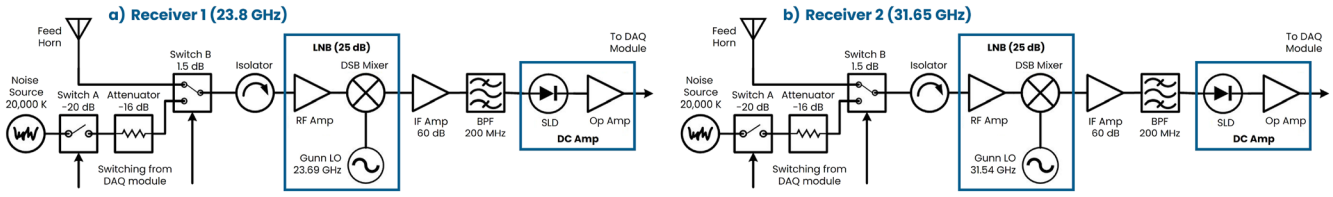

FIG. 5. Original WVR-III RF electronics of the receivers are identical, but each follows the respective frequency requirements.

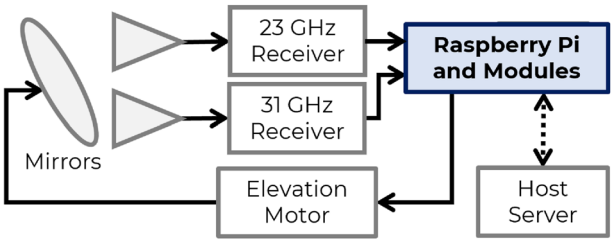

FIG. 6. New WVR-III+ architecture. The incorporation of the RPi computer allows the elimination of multiple modules shown in Fig. 4.

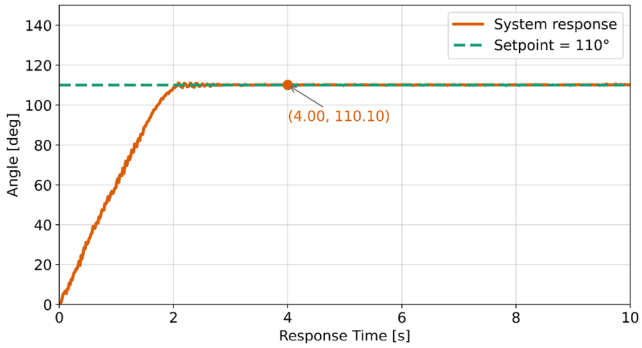

FIG. 8. Example of a step-response of the elevation control system for a setpoint of 110°. As expected, the setpoint is achieved in less than 4 s within the allowable tolerance.

were originally done by distinct modules. Moreover, an SBC provides powerful computational capabilities for data processing and analysis in a compact design, in contrast to the previous external personal computer.

IV. DETAILED REFURBISHMENT EFFORTS

The refurbishment of the former WVR-III presented several technological and logistical challenges, as the instrument had been disabled for more than a decade due to technical failures. In addition, given the changes in HartRAO management, technical documentation was lost during this period. Despite this, we managed to continue with the repair of the WVR-III and we detail the work performed in this section.

The refurbished architecture of the WVR-III+ (see Fig. 6) is based on a centralized processing core: the Raspberry Pi 3 B+ computer[28] (hereafter, RPi) and its peripherals to manage the main radiometer tasks.[29] In addition to replicating the original WVR-III working scheme, this new system also provides autonomy to the tipping process, software customization, and real-time data processing through the implementation of the SBC. Furthermore, the user is able to remotely communicate with the instrument for debugging, data consulting, and system management.

A. Motor control

The old WVR-III mechanical system was based on a DC-motor control loop for the elevation angles of tipping mirrors. This control system used an inclinometer as the feedback element, a CPLD as the control unit, and a DC motor as the actuator element. Due to challenges in modifying the mechanical structure, we chose to keep the servomechanical elements but replace the control unit and the feedback element in the chain. Thus, we implement new modules in the WVR-III+; the LSM9DS1 Inertial Measurement Unit as the feedback element, the RPi as the control unit, and a pulse width modulation interface plus an H-bridge based power stage as part of the actuator element, as shown in Fig. 7.

This scheme provides a closed-loop control over the elevation mechanism. The control law was designed to achieve an overdamped response with a rise time ≤2.5 s, a settling time ≤4 s, and an allowable tolerance of ±0.5°. An example of the step-response is shown in Fig. 8.

Despite the ~5° HPBW of the radiometer feed horns being 50 times larger than the uncertainty required by the control system, a high-precision pointing is required for the control system. Elevation angle deviations of > 1° lead to errors of ≳ 2.5 K in the calibration of a K-band radiometer.[26] Thus, a pointing precision of <1° is suitable for this type of radiometric system.

To evaluate the actual pointing precision of the system, we analyze the mean (μ) and the standard deviation (σ) of the angle achieved for a given setpoint angle using a set of eight elevations. The data consist of a single day with 3780 elevations taken at 90°, 60°, 50°, 45°, 40°, 35°, 30°, and 28°, which were continuously repeated during the day. Following the data in Table II, the control system works within the estimated allowable tolerance, achieving the setpoint with a typical uncertainty of ±0.1°.

Although the mechanism allows the motion of elevation angles from 0° to 180°, as shown in Fig. 9(a), the user-defined elevation angles can only vary from 10° to 90° (i.e., for either side from the horizon to the zenith), as shown in Fig. 9(b). This restriction is due to the definition of air mass and its use in the reduction algorithms: if θ is the elevation angle, then the air mass m is defined as

$$m = \sec(90^\circ - \theta). \quad (5)$$

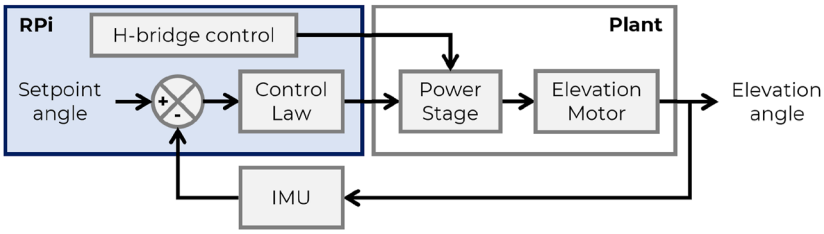

FIG. 7. Newly implemented elevation control system of WVR-III+.

TABLE II. Statistics of the implemented control system.

Setpoint	μ	σ	Scans	Setpoint	μ	σ	Scans
90.0°	89.82°	0.05°	473	40.0°	40.12	0.09°	472
60.0°	60.10°	0.11°	473	35.0°	35.14°	0.08°	472
50.0°	50.12°	0.10°	473	30.0°	30.12°	0.09°	472
45.0°	45.11°	0.10°	473	28.0°	28.15°	0.06°	472

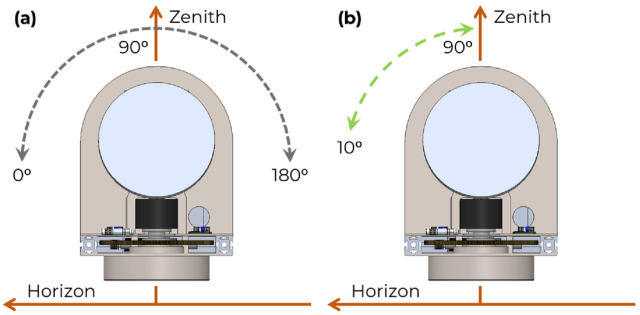

FIG. 9. Side view of a rendered model of the WVR-III+. (a) Natural and (b) permissible motion of the elevation mechanism.

The 10° limit follows from two considerations. First, in practice, elevation angles near the horizon can encounter terrain obstacles, leading to erroneous measurements. Second, the original elevation mechanism suffers from a manufacturing defect, which causes the locking of a pulley when the mirrors fall to exactly 0° (or 180°) elevation.

Despite the mechanical capability of WVR-III+ to azimuth rotation, we did not implement a control system for it. For the present, we will operate the WVR-III+ at a single fixed azimuth; an extension of the elevation control concept to the azimuth may be made in the future.

B. Signal acquisition

The WVR+III consists of two 200 MHz channels centered at 23.8 and 31.65 GHz, with noise power originally measured over an integration time of 100 ms in each channel (see Fig. 5 and Table I). As mentioned throughout Sec. III, the various RF components were all in working condition, so we kept the front-end architecture and components in the new design. However, a new signal conditioning stage was required to process the receiver output by using the RPi. Furthermore, the switches of the receivers (also shown in Fig. 5) required a new control interface because the original was removed from the instrument.

1. Signal conditioning

The output voltage from the power detectors at the end of the receivers were originally acquired by the DAQ module and sent to the host computer through the RS-485 interface (see Fig. 4). These outputs have a dynamic range of 10 V (0–10 VDC). Since the RPi cannot directly acquire analog signals, it was necessary to implement an external analog-to-digital converter (ADC) for signal acquisition. The newly implemented ADC is the ADS1115 board,

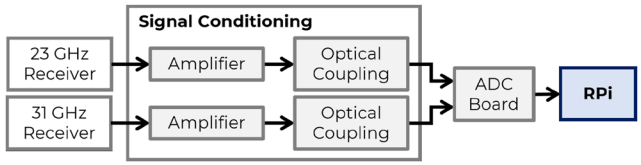

FIG. 10. Signal conditioning stage chain.

which provides 16-bit conversion, four-channels, programmable gain amplifiers, and I2C serial communication interface for data transmission.

The ADS1115 has been configured to provide a full-scale range of 4 V (0–4 VDC), with a resolution of 61 μV for a 16-bit acquisition mode, and a default sampling rate of 128 Hz (modifiable up to 860 SPS). It became evident that we could not directly connect the receivers' outputs to any of the ADC channels because of a mismatch in dynamic ranges. Therefore, we designed an analog signal conditioning circuit between the receivers and the ADC board, converting the 10 V range of the receivers to the 4 V range of the ADC prior to digitization. Figure 10 shows the implemented signal conditioning stage, which primarily consists of operational amplifiers (providing the gain) and optical isolation of the primary stages of the chain. TL081 operational amplifiers were used in the *Amplifier* stages, and the HCNR201 chips were used in the *Optical Coupling* stages. Analog channels are sequentially acquired by the RPi, following the switching scheme discussed in Sec. IV B 2.

The frequency response of the conditioning stage was characterized to estimate the operable bandwidth and the practical gain. For this purpose, we made Bode plots of the overall conditioning stage; the frequency response is shown in Fig. 11. Following the plots, we obtain a gain of −7.33 dB for a 10 kHz bandwidth without a phase shift. The gain of the signal conditioning stage is digitally compensated for in the ADC readings made by the RPi.

2. Source switching control

The radiometric observations of the WVR-III+ follow the scheme addressed in Sec. II A, which means that the receivers sequentially observe three different noise power sources: the water vapor emission collected by the feed horn as the *sky*, the internal noise source power as the *hot load*, and the power of an attenuator as the *cold load*. The measurements obtained by observing these sources provide V_A, V_H, and V_C, respectively.

Originally, the DAQ module controlled switches A and B inside the receivers, represented by the external lines connected to such switches in Fig. 5. For the new design, we implemented a relay-based interface to control the switches. We use the scheme shown in Fig. 12, where four of the RPi's general purpose input/output pins (GPIO) are connected to transistor-driven relays: using the 2N2222 transistors and the Axicom V23079 relays.

The observation sequence of the radiometric measurements is shown in Table III (also see Fig. 5). Note that state 2 provides the noise power due to the attenuator as a termination load at room temperature (usually $\gtrsim$ 300 K), i.e., the *Cold Load*—the accurate temperature of the cold load is measured by transducers B and A, as described in Sec. IV C 2. State 4 provides the *Hot Load* noise power

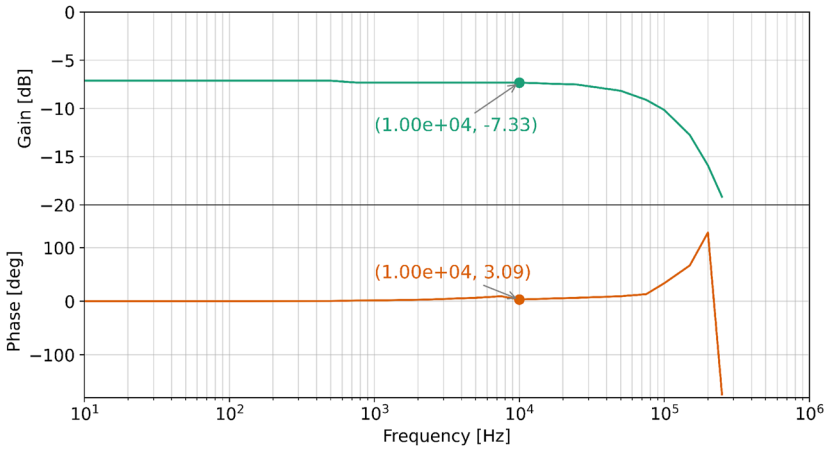

FIG. 11. Frequency response for a single channel of the signal conditioning stage. Note how the gain and phase remain constant to roughly 10 kHz.

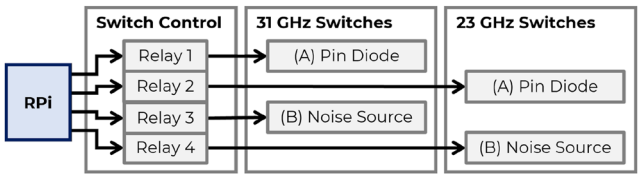

FIG. 12. Front-end switch control chain. Relays provide galvanic isolation of the front-end electronics from the rest of the system.

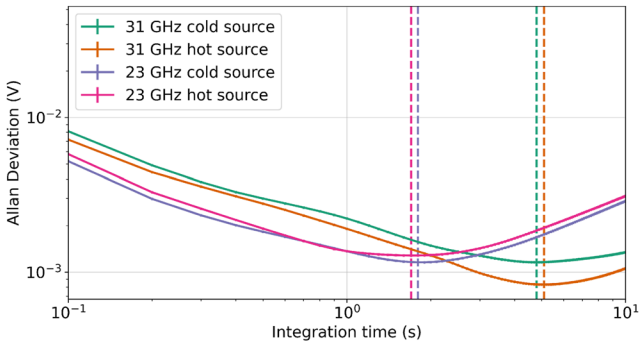

FIG. 13. Measured Allan variance for both receiver channels. The cold source values indicate the overall receiver stability, while the hot source values indicate the noise source stability.

TABLE III. Single radiometric observation by relay sequence.

State[a]	Switch A[b]	Switch B[c]	Power source	Int. Time[d] Rec. 1 | Rec. 2
1	OPEN	UP	Feed horn (*Sky*)	2 s | 5 s
2	OPEN	DOWN	Attenuator (*Cold*)	2 s | 5 s
3	CLOSED	UP	Feed horn (*Sky*)	⋯
4	CLOSED	DOWN	Noise source (*Hot*)	2 s | 5 s

[a]State 3 is not used.
[b]OPEN is the noise source connected to the path (1 dB insertion loss); CLOSED is the noise source isolated (20 dB) to the path.
[c]UP is connected to the antenna feed horn; DOWN is connected to the noise source path; see Fig. 5.
[d]User definable.

as a cascade combination of the noise source and the attenuator (≈1000 K).

The acquisition cycle of the radiometer proceeds with the three measurements of States 1, 2, and 4 in both receivers up to a maximum 5 s per state and another 5 s allocated for processing. This results in a maximum measurement time of 20 s per elevation angle. With six elevation measurements used in the tip curve, the total time required to estimate zenith opacity is less than 2 min, which is fast enough assuming that the time variability of the atmosphere is on the order of several minutes.[22]

3. Radiometer stability

The Allan variances of the 23 and 31 GHz channels (see Fig. 13) were measured to determine the receiver and noise source stabilities. The measurements were made over a 3-min interval with 100 ms sampling. The Allan times for the 23 GHz channel are 1.7 and 1.8 s for the cold and hot loads, respectively. For the 31 GHz channels, the corresponding times are 4.8 and 5.1 s. The cold load values can be considered to be the Allan variance of the receiver, while the hot load values are indicative of the stability of the noise source. These Allan times allow for a measurement sensitivity of $\lesssim 0.2$ K.

4. Radio frequency interference

To determine whether the RPi generates any harmful radio frequency interference (RFI), we measured RF levels close to the RPi board using a near-field probe connected to a Rohde & Schwarz FSW50 spectrum analyzer. The spectra shown in Fig. 14 represent five different tested locations using the probe: near the RPi power supply components (*turquoise*), above the CPU chip (*orange*), near the RJ-45 Ethernet connector (*violet*), and two arbitrary locations over the board (*magenta*, *lime*).

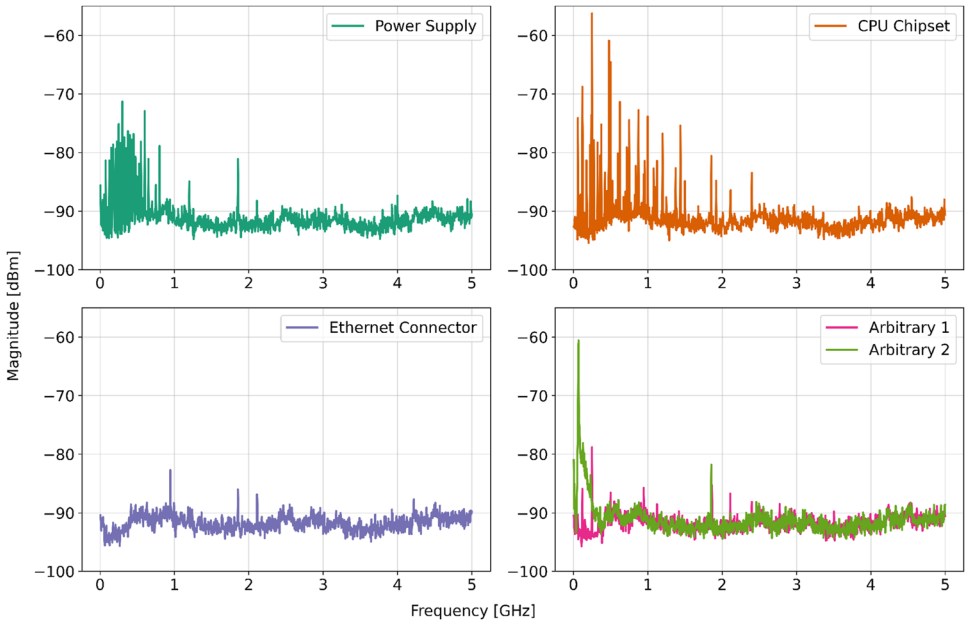

FIG. 14. Measured RFI components generated by the RPi board. With the probe at a distance greater than 2 or 3 cm, no signals were detected above the −90 dBm noise floor.

As seen in the spectrum, there is unlikely to be any emission in the RF bands; however, emission in the 110 MHz IF band is possible. Given a 200 MHz integration bandwidth, a typical T_A of 290 K would result in power levels of around −63 dBm at the input of the IF amplifier, where the system would be more susceptible to RFI. Although this is comparable with the levels measured above the CPU of the RPi, a minimum of 70 dB of shielding is easily achieved by the receiver's metal enclosure and braided ground coaxial cable, resulting in a negligible contribution of RFI to measurement error.

C. Complementary sensors

In addition to the modules discussed so far, there is a sensor suite in the WVR-III+ that monitors weather variables and receiver temperatures. Here, we describe the purpose of these complementary sensors.

1. Weather station

Several PWV or path delay retrieval algorithms depend upon the meteorological conditions at the radiometer site. Hence, apart from the radiometric measurements, a radiometer is often provided with a weather station. One of these systems was included in the original WVR-III, but was an external system, as shown in Fig. 4. This weather station was consulted via a serial protocol by the host computer, where the data were processed simultaneously with the radiometric data.

We replaced the weather station with a compact weather sensor incorporated into the radiometer structure, providing for greater compactness. A suitable solution for the WVR-III+ was the BME280 module, used to measure the same variables as the weather station of the original WVR-III: the air temperature, relative humidity, and barometric pressure. This modular sensor is connected as a slave to the RPi and consulted via the I2C protocol (see Fig. 15).

FIG. 15. Weather transducer.

2. Receiver temperatures

Radio frequency receivers are susceptible to gain fluctuations. These fluctuations directly affect the overall sensitivity of the radiometer: gain fluctuations on timescales longer than intrinsic calibration timescales (for example, via a Dicke switch) will decrease the radiometer sensitivity. Among the various origins of these phenomena is the operating temperature of the receiver; a good radiometer design must include some means for stabilizing the operating temperature.

The WVR-III was originally provided with a heating system that kept the receiver boxes at a controlled operating temperature with the intention of minimizing receiver gain fluctuations. This system consists of a temperature controller module, in which a setpoint value was introduced by the user. Then, the controller turned on two resistive heaters to change the temperature of the baseplates of each receiver. Finally, the control loop was fed back through a PT100 temperature sensor located on the surface of the 23 GHz receiver baseplate. This system was independent of the radiometer architecture and its tasks, so the user could adjust the control system before and during radiometric operation. Apart from the controller's sensor, three other PT100 sensors were used to monitor temperatures inside the receiver enclosures: two on each of the baseplates of both receivers and one more only in the 23 GHz receiver noise source case. Temperature data were collected by the DAQ module and reported to the host computer.

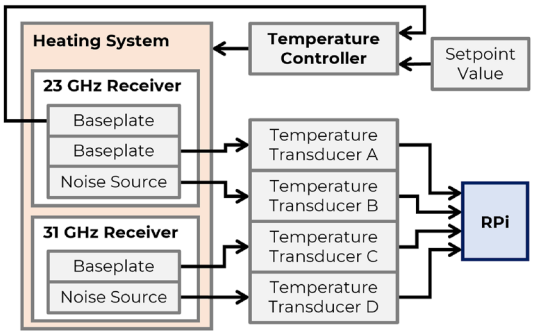

FIG. 16. WVR-III+ heating system allows a complete monitoring of the instrument temperatures, as well as a simultaneous heating action on both receivers. Each *Baseplate* and *Noise Source* box included a PT100 temperature detector in that part of the receiver, and the components within the salmon-colored box share a single thermal path.

For the WVR-III+, we kept the heating system scheme, but replaced both the temperature control unit (due to out-of-date technology) and the temperature sensors inside the receiver boxes. In addition, a fifth temperature sensor was added in the 31 GHz noise source case, as shown in Fig. 16. The current controller is a Shinko BCS2R10, and all five sensors are PT100 type. The new temperature transducers are the MAX31865 modules, which read the PT100 signals and send the data to the RPi via the SPI protocol.

The heating control continues to be a separated process from the radiometric tasks. The detector layout now allows for monitoring and comparison of the temperature changes in the baseplates and noise sources of each receiver. In this way, we have uniform monitoring of the environment inside the receivers for possible corrections in data retrieval and to prevent damage to the hardware due to extreme temperatures and avoiding condensation at dew point temperatures. If any of the five temperature transducers measures below 0 °C or above 50 °C, a report is sent to the system logger and the radiometric tasks are stopped (also see Sec. IV E).

Since the temperature controller only allows heating and not cooling, the *Setpoint Value* shown in Fig. 16 is adjusted depending on the weather of the site and should be changed during the year. This setpoint should be approximately equal to the maximum temperature expected at a given time of the year to avoid large fluctuations in the temperature to be controlled. For instance, a setpoint T_{sp} lower than the outdoor temperature T_{amb} causes the control action to shut down until the setpoint is reached by natural cooling. This implies a significantly longer settling time than would be achieved with a controlled chiller. Depending on the time of day when the above-mentioned process occurs, it could be affected by sudden temperature changes between the sunrise and sunset. In contrast, $T_{sp} \approx T_{amb}$ means lower temperature differences in which there will be less settling time both active (for heating) and natural (for cooling).

As a review of the stability of noise sources in the WVR-III+, we analyze a week of data taken from April 21–28, 2024. As shown in Fig. 17, the voltages of the noise sources remain constant within one tenth of a volt around the average voltage. Note that despite the outdoor temperature gradients (from ~15 °C to ~35 °C) during the day, the overall system response is stable within the specified range in both receivers.

Comparison of the Allan time (see Sec. IV B 3) with the temperature stability indicates that temperature variations are substantially slower than any reasonable integration time, thus ensuring that temperature instabilities will not degrade the system sensitivity.

D. Power supplies

The efficient operation of various internal stages of the WVR-III+ depends on a stable bias supply, provided by a dedicated power supply card (custom-engineered) to deliver the required voltage and current to each subsystem. Currently, the WVR-III+ incorporates a primary and a secondary power supply: the former provides AC–DC conversion and the latter consists of DC–DC converters.

The primary power supply (PPS) converts the AC power line to DC-power required by the secondary power supply (SPS), the elevation mechanism and the heating system. The PPS is assembled in

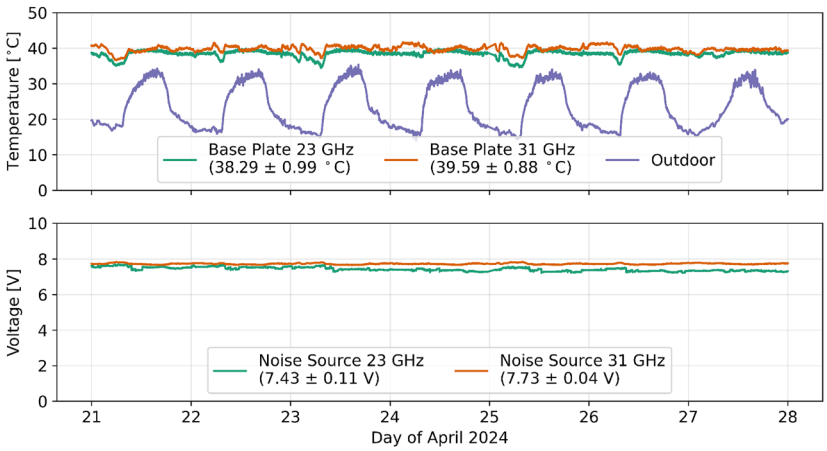

FIG. 17. Time series of radiometer temperatures (top panel) and noise sources voltages (bottom panel). Temperature deviations of 1 °C cause voltage drifts of ≈0.1 V. The outdoor temperature is shown as a reference of the daily gradients.

a separate metal box from the radiometer housekeeping and is connected using a 5 m circular connector power cable. The features of the PPS are shown in Table IV.

The custom SPS board draws a +12 V bias from the WVR-III+ PPS. The SPS consists of three DC–DC COSEL converters, two solid-state regulators, and two LM2596 modules, together with a Cincon DC–DC converter. Each radiometer channel requires its own voltage distribution, so the SPS board offers distinct voltage outputs for each channel. The SPS outputs and the modules where they are implemented are shown in Table V and are distributed as follows:

- The two +12 V outputs supply the LM2596 modules, which are special, high-stability DC–DC converters used to provide +6.7 V to the Gunn oscillators. They are needed due to the extremely low DC input impedance of the oscillators—around 4 Ω for the 23 GHz channel and 2.5 Ω for the 31 GHz channel. The converters thus provide 1.67 and 2.68 A for the two channels, respectively. The LM2596 modules can support these current levels without disturbing the low voltage values.
- The +15 V is delivered by an ECLB60-12S15 Cincon module, which takes the input +12 V and converts it into a stable voltage level of +15 V.

TABLE IV. PPS components of the WVR-III+.

Converter	Type	Input Power (W)	Output Voltage (VDC)	Output Power (W)	Supplies to
Mean well LRS-50-12	Switching	110	12	50	Elevation Mechanism
Traco ESP-180-12S	Switching	130	12	180	SPS
Intronic RT225-218	Linear	150	44	125	Heating System

TABLE V. SPS components of the WVR-III+.

Output voltage	Supplies to	Board terminal	RF channel (GHz)
+12 V	LM2596 module	3	23
+12 V	LM2596 module	5	31
+15 V	Op amp integrator	7	23
−15 V	Op amp integrator	9	23
+15 V	Op amp integrator	11	31
−15 V	Op amp integrator	13	31
−10 V	Switching control	15	23
−10 V	Switching control	17	31
+5 V	Switching control	19	23
+5 V	Switching control	21	31
+28 V	Noise source	23	23
+28 V	Noise source	25	31

- The −15 V output is generated by the ZUS101215 COSEL module in reverse configuration. In addition, the same −15 V are step-down to −10 V (required for the source switching board) by using an LM337 voltage regulator.
- The +5 V output is generated using the ZUS101205 COSEL module in a standard configuration.
- The +28 V output is obtained using the ZUW31215 COSEL module, which generates a symmetrical output of ±15 V. Using these values in a sum of voltage sources, a single output of +30 V is obtained, and latter adjusted to +28 V by the LM317 voltage regulator.

The Cincon and COSEL modules are supplied by the +12 V input and are excellent DC–DC converters that can maintain a stable output voltage signal despite possible disruptions at the voltage input. The LM337 and LM317 are stable voltage regulators, which can hold stable voltage levels with constant current.

Under normal operating conditions (considering the heating system on), the total power requirement of the radiometer is 390 W at maximum load.

E. Instrument control

The WVR-III+ is comprised of three main components to provide autonomy and high performance through the use of an SBC: the *hardware*, described in the previous sections and elsewhere;[29] the *firmware*, which allows communication between the SBC and peripherals; and the *software interface*, which performs the tip scans (sky surveys).

The *firmware* consists of Python-coded drivers that interact with the WVR-III+'s electronic components. The drivers are used to create a module that performs tasks, e.g., temperature system readouts or servo-mechanism control. The module is implemented as the script **wvrsa** and is executed on the RPi as the main control program. This program performs a tip scan using the new core and firmware to communicate with each subsystem for request and control data. The flow chart of **wvrsa** is shown in Fig. 18. At the beginning, the main program imports libraries and Python modules to control the WVR-III+ and the user defines a list with the desired elevation angles to scan, and the switching mode. Then, the program executes a set of hardware tests, including the following.

1. **Test servomechanism control:** sequentially runs two different elevation angles to check the correct functioning of the servomechanism.
2. **Test receiver temperatures:** confirms connection with the four temperature transducers inside the receivers by taking a single temperature reading and restricts the code execution within the operable range.
3. **Test RF acquisition:** checks if the receivers' outputs are within the linear operating regime (0–10 VDC) by taking a single ADC reading.

If these tests are successful, then the **survey** module begins; see Fig. 19(a). In case of errors, processing is passed to the **logger** module [see Fig. 19(b)] and the main program is stopped. The survey module performs the task of data acquisition, which includes setting up the servo-mechanisms, reading the weather variables, reading the receiver temperatures, and acquiring the RF signals for the switching

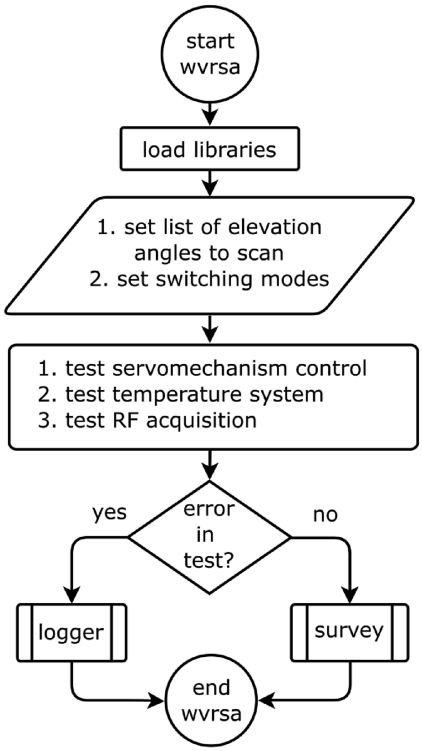

FIG. 18. *wvrsa* script is the main control code for the WVR-III+, coordinating the execution of the object codes to individual components of the instrument.

mode defined by the user. Finally, the measurements are saved into a CSV (comma-separated values) file. The internal functions of the modules shown in Fig. 19 are described in the following.

- **Servo-mechanism control**: manages a discrete-time controller for the elevation mechanism (see Fig. 7) and set the mirrors to the desired angle.
- **Weather station monitor**: requests ambient temperature, relative humidity, and barometric pressure measurements from the weather transducer (see Fig. 15).
- **Temperature system monitor**: obtains *n* samples specified by the user from each temperature transducer and computes the median (see Fig. 16). The result represents the reported temperature of each sensor.
- **RF signal acquisition**: used to digitize the output signals from both RF receivers (see Fig. 10) and manages the observation sequence shown in Table III.
- **Save data to file**: saves all measurements into a CSV file and stores them in the RPi.
- **Logger**: registers all events (errors, exceptions, and messages) that happen during **wvrsa** execution. The file gives information about these events, including when and where in the execution they occurred.

When a cycle of observations through the specified set of elevation angles is complete, i.e., to obtain a single-tip curve, the survey module is continuously executed. For a typical acquisition time of

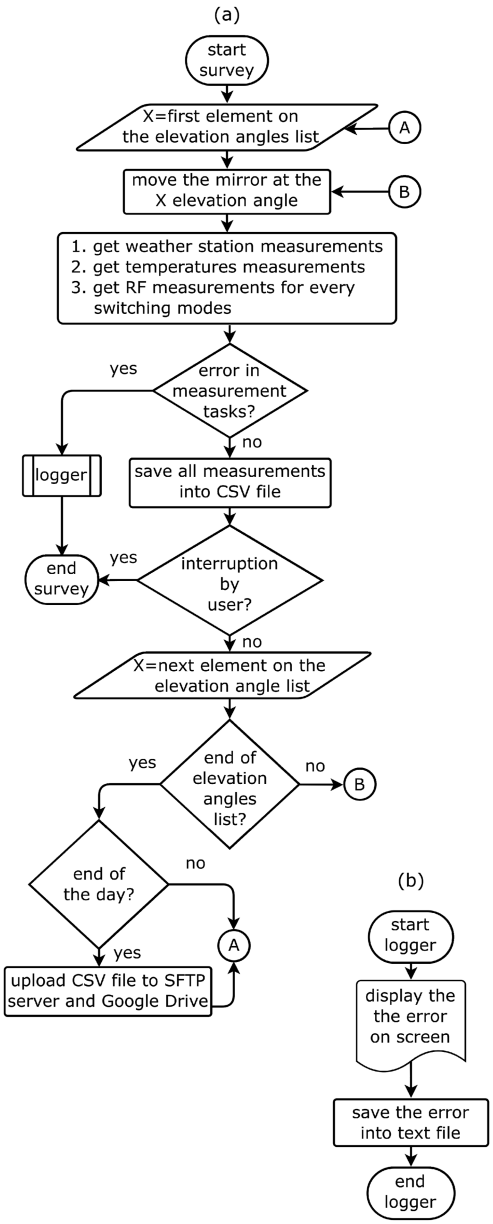

FIG. 19. (a) *Survey* module performs radiometric measurements. (b) The *logger* module saves errors, exceptions, and message events.

20 s per elevation, a daily dataset is expected to contain about 4320 rows of data, provided there are no significant software delays. The infinite loop can be broken only if the user interrupts the program (usually with a control-c keystroke) or a critical error arises during data acquisition. At the end of a 24 hour period, the program executes an automated procedure to upload a copy of the CSV file to a Secure File Transfer Protocol server and Google Drive storage account to backup the measurements.

F. Communication

The WVR-III+ system is mainly controlled by the RPi, as described in Sec. IV. An SBC-based solution offers several hardware and software benefits for communication, which we took advantage of for the new WVR-III+ design. In this sense, the Raspbian operating system (version 9, *Stretch*) of the RPi allows communication with other computers for both internal and external networking by using Ethernet, WiFi, or 4G-LTE modules. Currently, the Internet connection is provided via the Ethernet port, which is used to upload all data files to cloud services for storage and access by the research team. Figure 20 shows the communication diagram of the system, including the serial interfaces and the network connection.

V. WVR-III+ COMMISSIONING

A. Radiometer features

The renewed WVR-III+ provides the radiometric characteristics listed in Table VI. Note that RF features are preserved from the original WVR-III front-ends.

The Allan variance measurements yielded maximum integration times of 1.8 and 5.1 s for the 23 and 31 GHz channels, respectively. Comparing these results with the integration times of 2 and 5 s applied in practice (see Table III) suggests that the WVR-III+ can be considered stable over the integration periods, thus synchronous calibration schemes are superfluous. Furthermore, since the WVR-III+ can achieve an ideal temperature sensitivity of ~0.2 K, and that a typical K-band PWV sensitivity[8,12] lies ~0.5 K/mm, the radiometer would be able to detect PWV changes of 1 mm for a signal-to-noise ratio of 10.

Generic system specifications of the WVR-III+ are shown in Table VII.

As mentioned in the literature,[26] a deviation of ±1° in the desired elevation angle leads to calibration errors (rms) up to 3.43 K at 23.8 GHz and up to 0.1 K at 31.65 GHz. In comparison, the new WVR-III+ system can perform tip scans with an angular tolerance of ±0.1°, which is accurate enough for the calibration process.

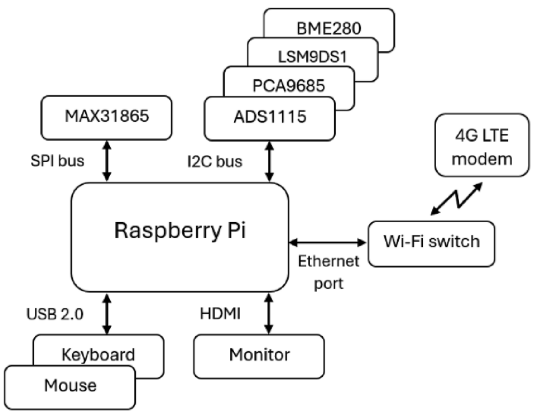

FIG. 20. RPI-based core of the WVR-III+ offers several ways to communicate with external devices, either for data export or remote maintenance.

TABLE VI. Radiometric specifications of the WVR-III+.

Feature	Receiver 1	Receiver 2	Units
Center frequency	23.8	31.65	GHz
Bandwidth	200	200	MHz
Noise temperature	700	900	K
Integration time	2	5	s
Noise temperature per unit bandwidth	3.5	4.5	K/MHz
Temperature sensitivity	200	200	mK
HPBW	4.3	5.1	°

TABLE VII. Generic specifications of the WVR-III+.

Feature	Value	Units
System core	Raspberry Pi 3 B+	···
Operative system	Raspbian 9	···
Acquisition time	20	s
Per tip scan (max)		
Pointing precision	±0.1	°
Temperature stability	±1.0	°C
Input voltage	220	V(AC)
AC power (max)	390	W
DC power (max)	355	W
Operating temperature	0–60	°C
Weight	50	kg

FIG. 21. Landscape of the H.E.S.S. site and our team installing an additional radiometer in March 2024. Radiometer station (*left*); Mt Gamsberg (*background center*); and H.E.S.S. telescopes (*right*).

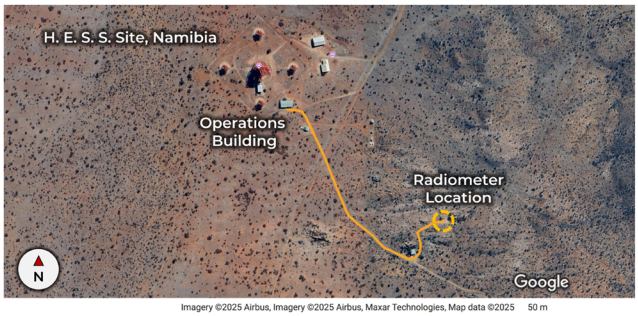

FIG. 22. Aerial view of the H.E.S.S. site. Radiometers are installed together on a hill, 650 m away (*yellow path*) from the H.E.S.S. operations building.

FIG. 23. Remote sensing instruments installed at H.E.S.S. From left to right panels: WVR-III+, Survey 3, solar panel, and GNSS station. Note that the radiometers are pointed toward the south because of the unobstructed view to the horizon, which favors the measurements.

The temperature stability of the heating system achieves around 1 °C around the setpoint, but can increase for larger outdoor temperature gradients. To ensure this stability, the WVR-III+ must operate in an ambient temperature range of 0–60 °C.

A 390 W dissipation at a maximum load suggests that the WVR-III+ will probably require a high-power converter for remote sites where a power line is not provided.

B. Current status

The African Millimeter Telescope project proposes to place a millimeter-wave observatory on the Gamsberg Plateau, which is located 40 km from the H.E.S.S. Observatory (see Fig. 21) in Khomas, Namibia. This makes the H.E.S.S. facilities an ideal deployment site for the initial logistics of the AMT. As a starting point, we placed the WVR-III+ at this site to evaluate the atmospheric conditions in the cm-band and also the behavior of the instrument under remote site conditions.

The WVR-III+ was installed at H.E.S.S. (1859 m elevation) by the Observatory's technical staff in mid-2022. Currently, this radiometer is located on a small rise, just over a half kilometer from the Observatory buildings (a map is shown in Fig. 22). The

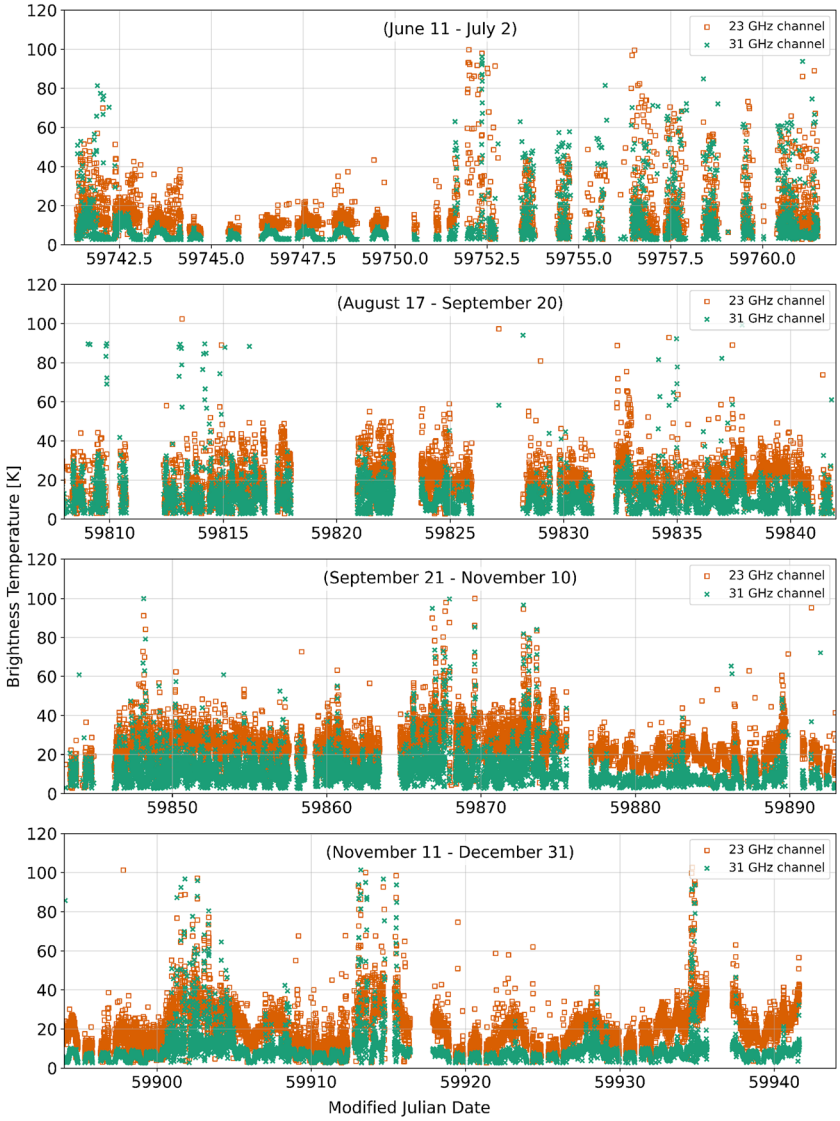

FIG. 24. Atmospheric brightness temperature time series at the 23.8 GHz (*orange*) and the 31.65 GHz (*turquoise*) radiometric channels during four different time windows of 2022 at the H.E.S.S. site. Due to a period of maintenance, the WVR-III+ did not take data from early July to mid-August.

radiometer is installed along with other remote sensing instruments, which are powered by a solar panel station and connected to the Internet via a 4G network of a Namibian commercial supplier.

The WVR-III+ is currently monitoring the water vapor concentration at the H.E.S.S. site (see Fig. 23), alongside the Survey 3 radiometer, which was previously used for site characterization in Mexico.[10,30] The Survey 3 is also a water vapor radiometer, but with a single channel at 210 GHz (in the wing of the 183 GHz water vapor emission line). Data from both radiometers are uploaded to the cloud for data retrieval and analysis by team members in Mexico, South Africa, and Namibia, providing a broad overview of the atmospheric variables at H.E.S.S.

C. H.E.S.S. Site measurements

Figure 24 shows the time series of atmospheric thermal emission, generated with data taken with the WVR-III+ installed on the surroundings of the H.E.S.S. site. Various atmospheric emission models[31,32] suggest that water vapor densities of <2 g/cm^2 (or $PWV = 20$ mm) lead to atmospheric brightness temperatures of <30 K in the K-band. As can be seen in Fig. 24, the brightness temperatures at the two frequencies are within those ranges, with higher values at 23.8 GHz than at 31.65 GHz. Both frequencies have the same temporal pattern, showing larger values in the middle of the day and lower values in the morning and evening. Such measurements are also consistent with the PWV values reported in the literature[33–35] for the H.E.S.S site, where PWV values of ~5 mm and ~35 mm are expected during the driest (May to September) and the wettest (October to April) seasons, respectively. A relationship between the brightness temperature measured with the WVR-III+ and the PWV, specific to this site, has yet to be determined.

VI. CONCLUSIONS

The current WVR-III+ system presents several improvements to the WVR-III from which it is derived. We have refurbished the acquisition, sensors, and control systems of the radiometer along with the software for data acquisition, control, and data reduction. In the process, we implement technology based on Python and Raspberry Pi, providing better autonomy, accessibility, and customization. Given the computational capabilities of this SBC, the WVR-III+ is capable of performing retrieval algorithms immediately at the end of the day. At present, our team is developing a new process to run natively on the RPi, but for the moment, the data analysis is done offline. The WVR-III+ refurbishment provides an extension of the useful life of this instrument for at least 5 more years. However, it is important to keep the front-end system under constant monitoring as this part of the radiometer is about two and a half decades old.

The preliminary results of field measurements are at the H.E.S.S facility. An observatory in Namibia validates the proper functioning of the refurbished system and the data reduction techniques. The WVR-III+ will take atmospheric data for the statistical analysis of the water vapor content at the H.E.S.S. site and other potential radio astronomical sites, such as Mt. Gamsberg, over the next few years. A complete development and discussion on this point will be presented in a future paper.

Finally, this work is a demonstration of the success of the South Africa–Mexico Bilateral Programme on Water Vapor Radiometry with the involvement of the University of Pretoria and the South African Radio Astronomy Observatory from South Africa, the National Institute of Astrophysics Optics and Electronics, the Institute of Astronomy-UNAM, and the Institute of Radio Astronomy and Astrophysics-UNAM from Mexico.

ACKNOWLEDGMENTS

This work was carried out with the financial support of the National Research Foundation (NRF) of South Africa and the Consejo Nacional de Humanidades, Ciencias y Tecnologías (CONAHCyT) of México under the South Africa–Mexico Joint Science & Technology Research Collaboration with Project Nos. UID114676 (NRF) and 291778 (CONACyT) granted from 2018 to 2024. The project was also supported by the DGAPA-UNAM under Project Nos. IT100318 and IT101622 and by the Institute for Radio Astronomy and Astrophysics. We acknowledge the invaluable staff support offered by the Hartebeesthoek Observatory and the High Energy Spectroscopic System. The authors thank colleagues at the University of Namibia and Radboud University for logistical support. Finally, we thank the referees whose suggestions improved the quality of this work.

AUTHOR DECLARATIONS

Conflict of Interest

The authors have no conflicts to disclose.

Author Contributions

J. Cuazoson: Formal analysis (equal); Methodology (equal); Software (equal); Visualization (equal); Writing – original draft (equal). **D. Hiriart**: Conceptualization (equal); Resources (equal); Writing – original draft (equal); Writing – review & editing (equal). **T. Stander**: Conceptualization (lead); Funding acquisition (equal); Writing – original draft (supporting). **R. Botha**: Resources (supporting); Validation (supporting). **J. Contreras**: Data curation (lead); Software (equal); Validation (supporting); Writing – original draft (supporting). **D. Ferrusca**: Methodology (supporting); Supervision (lead); Validation (lead). **E. Ibarra-Medel**: Methodology (supporting); Writing – original draft (supporting); Writing – review & editing (supporting). **S. Kurtz**: Funding acquisition (equal); Project administration (lead); Writing – review & editing (equal). **R. Neate**: Data curation (supporting); Methodology (supporting); Validation (supporting). **D. Rojas**: Validation (supporting); Visualization (equal); Writing – review & editing (equal). **M. Velázquez**: Formal analysis (supporting); Methodology (supporting); Supervision (supporting).

DATA AVAILABILITY

The data that support the findings of this study are available from the corresponding author upon reasonable request.

REFERENCES

[1]T. Stander, R. Deane, D. I. L. de Villiers, A. de Witt, D. Ferrusca Rodriguez, D. Hiriart, S. E. Kurtz, F. van den Heever, and M. V. de la Rosa Becerra, Proc. SPIE **11445**, 193 (2020).

[2]D. Hiriart, P. F. Goldsmith, M. F. Skrutskie, and L. Salas, Revista Mexicana de Astronomia Y Astrofisica **33**, 59 (1997).

[3]A. Otárola, D. Hiriart, and J. E. Pérez-León, Revista Mexicana de Astronomia Y Astrofisica **45**, 161 (2009).

[4]B. Nikolic, R. C. Bolton, S. F. Graves, R. E. Hills, and J. S. Richer, Astron. Astrophys. **552**, A104 (2013).

[5]M. Backes, C. Müller, J. E. Conway, R. Deane, R. Evans, H. Falcke, R. Fraga-Encinas, C. Goddi, M. Klein Wolt, T. Krichbaum, G. MacLeod, V. A. Ribeiro, F. Roelofs, Z. Q. Shen, and H. J. van Langevelde, in *Proceedings of the 4th Annual Conference on High Energy Astrophysics in Southern Africa—PoS(HEASA 2016)* (PoS, 2017), Vol. 275, p. 29.

[6]National Radio Astronomy Observatory, Next generation very large array (ngVLA), 2024, https://ngvla.nrao.edu/, accessed 22 August 2024.

[7]J. Cernicharo, *Water, Vibrational and Rotational Transitions* (Springer, 2014), pp. 1–4.

[8]M. C. Wiedner, "Atmospheric water vapour and astronomical millimetre interferometry," Ph.D. thesis, University of Cambridge, UK, 1998.

[9]B. Deuber, N. Kampfer, and D. G. Feist, IEEE Trans. Geosci. Remote Sens. **42**, 974 (2004).

[10]D. Ferrusca, J. Contreras, J. Cuazoson, D. Hiriart, E. Ibarra-Medel, S. Kurtz, D. Rojas, and M. Velázquez, Proc. SPIE **12182**, 121824F (2022).

[11]R. Hills, H. Gibson, J. Richer, H. Smith, V. Belitsky, R. Booth, and D. Urbain, "Design and development of 183 GHz water vapour radiometers," ALMA Memo No. 352, 2001.

[12]A. Gill, R. J. Selina, B. J. Butler *et al.*, "A study of the compact water vapor radiometer for phase calibration of the Karl G. Janksy Very Large Array," EVLA Memo No. 203, 2017.

[13]M. Frounchi, "Millimeter-wave quadrature receivers for atmospheric sensing and radiometry," Ph.D. thesis, Georgia Institute of Technology, 2021.

[14]M. T. Behrens and T. Stander, Proc. SPIE **11445**, 1144580 (2020).

[15]R. Neate and T. Stander, Proc. SPIE **13094**, 130945D (2024).

[16]K. Cortes, R. Reeves, P. Kangaslahti, W. Ramírez, L. Mora, P. Cartes, D. Arroyo, B. Molina, G. Burgos, and M. Figueroa, in CHILEAN Conference on Electrical, Electronics Engineering, Information and Communication Technologies (CHILECON), 2017.

[17]L. Pena Contreras, "A 22 GHz pseudo-correlation water vapor radiometer," M.Sc. thesis, University of Concepcion, Chile, 2023.

[18]E. Pottiaux and R. Warnant, in EUREF Proceedings of the EUREF 2002 Symposium in Ponta Delgada (Azores Islands), 2002.

[19]T. Stander, D. I. L. de Villiers, A. de Witt, D. F. Rodriquez, D. Hiriart, S. E. Kurtz, F. v. D. Heever, and M. V. d. L. R. Becerra, in *2022 International Conference on Electromagnetics in Advanced Applications (ICEAA)* (IEEE, 2022), pp. 282–286.

[20]D. Ferrusca Rodriguez, J. Cuazoson, J. Contreras, D. Hiriart, E. Ibarra Medel, S. E. Kurtz, T. Stander, and M. V. de la Rosa Becerra, Proc. SPIE **11445**, 195 (2020).

[21]A. Brown, P. Chadwick, H. Dickinson, C. Hadjichristidis, I. Latham, R. Le Gallou, T. McComb, S. Nolan, A. Noutsos, K. Orford *et al.*, in *29th International Cosmic Ray Conference (ICRC29)* (Tata Institute of Fundamental Research, 2005), Vol. 5, p. 403.

[22]M. A. Janssen, *Atmospheric Remote Sensing by Microwave Radiometry*, *Wiley series in remote sensing* (Wiley, New York, 1993).

[23]E. S. Claflin, S. C. Wu, and G. M. Resch, Deep Space Network Prog. Rep. **48**, 22 (1978).

[24]S. C. Wu, Deep Space Network Prog. Rep. **43**, 67 (1977).

[25]J. B. Costales, G. F. Smoot, C. Witebsky, G. de Amici, and S. D. Friedman, Radio Sci. **21**, 47, https://doi.org/10.1029/rs021i001p00047 (1986).

[26]Y. Han and E. R. Westwater, IEEE Trans. Geosci. Remote Sens. **38**, 1260 (2000).

[27]E. R. Westwater, S. Crewell, and C. Mätzler, URSI Radio Sci. Bull. **2004**, 59.

[28]Raspberry Pi Ltd., Raspberry Pi 3 Model B+, 2024, https://www.raspberrypi.com/products/raspberry-pi-3-model-b-plus/, accessed 22 Dec 2024.

[29]J. Cuazoson, D. Ferrusca, J. Contreras, E. Ibarra-Medel, M. Velázquez, S. Kurtz, and D. Hiriart, in *2021 18th International Conference on Electrical Engineering, Computing Science and Automatic Control (CCE)* (IEEE, 2021), pp. 1–6.

[30]D. Hiriart, in I. Cruz-Gonzalez, R. Avila, and M. Tapia (Eds.) *Revista Mexicana de Astronomia Y Astrofisica Conference Series*, 19 (Revista Mexicana de Astronomía y Astrofísica, 2003), pp. 90–96.

[31]J. W. Waters, *Methods in Experimental Physics*, 12 (Academic Press, 1976), p. 142.

[32]B. Lew and J. Uscka-Kowalkowska, Mon. Not. R. Astron. Soc. **455**, 2901 (2015).

[33]F. F. Macucule and M. Backes, *IAU General Assembly* (IAU, 2024), p. 1864.

[34]M. Backes, F. Macucule, and L. Frans, in *High Energy Astrophysics in Southern Africa 2023* (PoS, 2024), Vol. 3.

[35]L. Frans, M. Backes, H. Falcke, and T. Venturi, *IAU General Assembly* (IAU, 2024), p. 1778.